Modulating mechanical performances of metallic amorphous materials through phase gradient

Yunlong Guan [a], Yunjiang Wang [b], Weidong Song [a],[*]

[a] *State Key Laboratory of Explosion Science and Technology, Beijing Institute of Technology, Beijing 100081, China*
[b] *State Key Laboratory of Nonlinear Mechanics, Institute of Mechanics, Chinese Academy of Sciences (CAS), Beijing 100190, China*

ARTICLE INFO

ABSTRACT

Increasing strength is usually at the cost of sacrificing ductility in structural materials. The tradeoff becomes even conspicuous in a category of metallic amorphous materials, the so-called metallic glasses (MGs) featured without any atomic-scale translational symmetry. Therefore, there remains little room for simultaneous optimization of strength and ductility in MGs through tailoring the morphology and kinetics of structural imperfections. Here we propose an alternative strategy for modulating the mechanical properties of MGs through introducing proper content of compositional or phase gradient inspired by the mechanistic strain gradient theory. We design two types of CuZr-based phase gradient metallic glasses (PGMGs) with different compositional concentration gradient directions in either continuous or stepped gradient form. Extensive molecular dynamics simulations demonstrate that phase gradient raises the concentration of mechanically stable icosahedral and icosahedron-like Voronoi polyhedra and, thus, increases the strength of MGs. In terms of plastic deformation, free volume mismatch between phases invalidates the autocatalytic activation mechanism of shear transformation zones, resulting in greater resistance to shear band propagation. The phase gradient also encourages branches of shear band and nucleation of multiple shear bands, which mechanism delocalizes deformation and postpones failure. These mechanisms lead to an improvement in the overall ductility of the PGMGs. The present strategy sheds light on evading the long-standing strength-ductility tradeoff in amorphous metals through extrinsic chemical and geometrical modulation that can be handled by appropriate thermal processing and fabrication technique.

1. Introduction

Since the first synthesis in 1960, metallic glasses (MGs) have received extensive attention due to their excellent mechanical properties, such as high strength, hardness, elastic limit, and elastic energy storage [1–13]. Regrettably, as an advanced material, MGs lacked widespread structural and functional applications up to date because of the limitations of their tensile ductility at room temperature. Recent experimental studies showed that modifying the composition and adjusting the processing methods (e.g., by changing annealing times or quenching rates) could somehow alter the mechanical properties of MGs [14–18]. The improvement in functions has been attributed to the changes in microscopic structure in terms of Voronoi polyhedra [19–22]. Therefore, the elemental ratio and processing technique can be changed in an appropriate way to tune the structure following a bottom-up philosophy to boost ductility. Nevertheless, the improvement remains limited.

To substantially enhance the ductility, some research groups proposed introducing a higher concentration of free volume in MGs. Based on this idea, researchers propose many strategies, such as nanoporous MGs [23–28] and nanoglasses [29–31]. For the nanoporous MGs, Şopu et al. [23] investigated the influence of void on the plastic deformation under uniaxial tension in the $Cu_{64}Zr_{36}$ MG. They revealed a necking-like homogeneous flow during the plastic deformation as void size decreases. Inoue et al. [25] also found that the adjustment of the void distribution can further promote the shear band delocalization in MGs, improving the overall ductility. However, the strength of these nanoporous MGs is lower than that of dense MGs.

As a new type of metallic glass, nanoglasses are typically produced by cold compacting of a large number of nano-scale MG particles obtained by the condensation of inert gases. Therefore, the structure of nanoglasses is very similar to polycrystalline, i.e., the existence of glass-glass interfaces (grain interfaces) except crystallites. The high free volume of nanoglasses is mainly derived from these grain interfaces. Based

on the tensile simulations of molecular dynamics (MD), Adibi et al. [30] observed homogeneous superplastic flow in nanoglasses when extremely small grain size was. With decreasing grain size, the grain interfaces became more and more uniformly distributed in the matrixes, which are preferred channels for plastic deformation so that the overall ductility of nanoglass is improved. However, the bonding between the atoms in the grain interfaces is weak, which makes the stress-carrying capacity of the matrixes more vulnerable. Therefore, nanoglasses with higher ductility were at the expense of their strength. In other words, strength and ductility are generally antithetical properties in MGs. As a result, taking account both strength and ductility are the current hot issues of in designing engineering relevant MGs.

One way to evade the strength-ductility tradeoff is the introduction of composite microstructures into MGs [32–35]. Following the strategy, Sha et al. [36] established a nanoglass with bimodal grain size, Albe et al. [37] designed the dual-phase nanoglasses, and Peng et al. [38] proposed the dual-phase Cu-Zr MGs. A compromise between strength and ductility was indeed achieved with these composite MGs. Importantly, an encouraging composite strategy to synergize strength and ductility in metallic materials is the application of gradient structure [39–42]. Yuan et al. [41] established some particle gradient nanoglasses (GNGs) and analyzed the tensile behaviors of these GNGs. They discovered that the gradient of grain size results in shear bands diffusion and delocalization, delaying the overall failure of the matrixes. Their GNGs achieved a mechanical synergy in strength and ductility. Zhao

et al. [42] introduced a stress gradient to MGs through experimental fabrication via surface imprinting. They discovered that the stress gradient structure simultaneously improves the strength and ductility of the MG matrix. Based on the success of these gradient strategies, we design two types of phase gradient architectures, combining various elemental ratios in the binary Cu-Zr MGs. These phase gradient architectures might also be a viable method that can synergize strength and ductility in the matrixes, the mechanism of which is the major aim of this study.

In this work, molecular dynamics (MD) simulations are employed to study the effects of the phase gradient microstructure on the mechanical properties of CuZr-based MGs. Through consolidating various elemental ratios perpendicular to the loading direction, we construct two types of phase gradient metallic glasses (PGMGs). The one type is an A-PGMGs in which the fraction of Cu varies first from 80% to 20%, and then from 20% to 80%. The other type is a B-PGMGs that the varying law of Cu ingredient is opposite to that of A-PGMGs. As a comparison, we also design continuous gradient and step gradient structures in each type of PGMGs. Section 2 depicts the methodologies, including the empirical potential for MD simulation, atomistic model, and thermodynamic conditions. Section 3 presents the simulation results and discussion of the microphysical causes of the macroscopic mechanical response. Finally, the relevant contribution and novelty of the gradient strategy are discussed in Section 4.
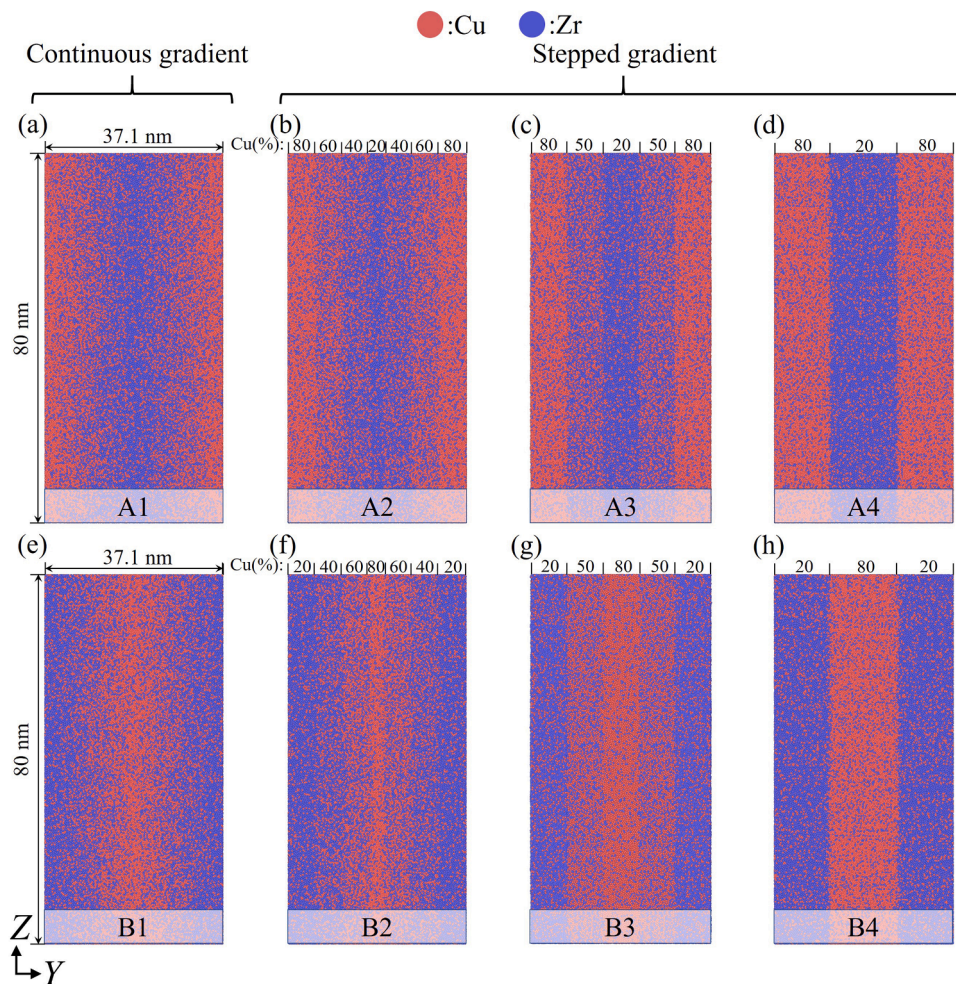

Fig. 1. Design of CuZr-based phase gradient metallic glasses. (a)-(d) in the top row are the A-PGMGs, and (e)-(h) in the bottom row are B-PGMGs. The samples on the left side possess continuous gradient architectures. On the right side, there are three stepped gradient samples for each type of the PGMGs.

2. Methodologies

The mechanical properties of PGMGs are analyzed by using the MD simulations package of LAMMPS [43]. The atomic interactions between Cu and Zr atoms are described by the embedded-atom method (EAM) potential developed by Mendelev et al. [44]. Cu-Zr glasses have been accurately described with this EAM potential because it undergoes a reasonable semi-empirical correction.

Fig. 1 shows all the PGMG models that we have established. First, a large number of homogeneous MG samples with different phases (elemental ratios) are generated in a thin-film geometry whose dimensions in the X-, Y- and Z-directions are 3 nm, 30 nm, and 80 nm, respectively. These phases include $Cu_{80}Zr_{20}$, $Cu_{70}Zr_{30}$, $Cu_{60}Zr_{40}$, ..., and $Cu_{20}Zr_{80}$, respectively. The boundary conditions during the sample establishment are periodic in three dimensions. 1000 ps and 2000 K are used as annealing time and temperature, respectively. Before reaching the 2000 K annealing temperature, the systems are carried out energy minimization to ensure the stability of structures. Importantly, the samples are quenched at a cooling rate of 10 K/ps to ensure the generation of a relatively stable amorphous structure. To build a continuous PGMG (ignoring the interfaces between the phases), the phase change in the gradient direction (Y-axis) should be as small as possible, so all MG samples are cut into slices of 3.0 nm thickness in the Y-direction. Subsequently, all the slices are combined in the Y-direction in a well-designed architecture to establish the aimed gradient for the elemental ratio. There are two types of continuous PGMGs. The one type is A1 that the proportion of Cu along the Y-direction on the free surfaces is maximum (80%) while that in the core is minimum (20%), as shown in Fig. 1(a). The other one is B1 that the fraction of Cu on the outer surfaces is minimum (20%) while that in the middle is maximum (80%), as displayed in Fig. 1(e). Additionally, to conduct a complete study of phase gradient structure, we also build three additional samples with different stepped amplitude for each type of the PGMGs, as presented on the right side of Fig. 1. Larger type number corresponds to higher stepped amplitude. E.g., the A4/B4 samples have only two phases: $Cu_{80}Zr_{20}$ and $Cu_{20}Zr_{80}$, respectively. Unlike the continuous PGMGs, these samples have identifiable phase interfaces and therefore are defined as stepped PGMGs. To equilibrate the atomic structure, the second annealing of 2500 ps is conducted at a temperature (600 K) near the glass transition temperature (T_g) for all PGMGs [38]. This annealing time is the shortest one required for constructing the continuous phase gradient. Afterwards, the samples are quenched again to 50 K and relaxed for another 200 ps. The constructions of all above MGs (melting, quenching, annealing, and relaxation) are carried out with an external hydrostatic pressure of 0 MPa and a timestep of 1 fs. The size of the PGMGs is approximately 3 (X) × 37.1 (Y) × 80 (Z) nm^3.

Then, we reset the Y-direction to the free surface to allow a shear offset. Uniaxial tensile test is performed along the Z-direction at a constant strain rate of 4×10^7 s^{-1}. The tension is carried out under the NPT ensemble at a constant temperature of 50 K. The condition of low temperature (50 K) emphasizes the pure mechanical response, because the micro MGs that experience a rapid quench on the order of picoseconds are generally more susceptible to thermal activation rather than the macro-glass structures in reality [45].

3. Results and discussion

The effects of phase gradient microstructure on the mechanical properties of CuZr-based MGs are presented in the following Sections. Section 3.1 presents the modulation of phase gradient on the strength of MGs. Besides, the reasons for the strength variation of PGMGs are exposed by using the features of atomic structure topology. In Section 3.2, the enhancement of the ductility of MGs by the phase gradient is revealed. Furthermore, the ductility improvement of PGMGs is explained through the difference in atomic-packing efficiency between phases. Finally, some possible experimental synthesis methods for

PGMGs are given in Section 3.3.

3.1. Tensile strength and local atomic structure

As it is known, the strength of material is most likely to be affected when a totally new structural design is introduced. Moreover, the effect of the atomic structure topology (the structure and number of atomic Voronoi polyhedra) is significant in terms of the strength of MGs. Therefore, in this section, the strength of PGMGs is systematically analyzed by the atomic structure.

Current research on the mechanical behaviors of the homogeneous MGs identifies a sharp drop of stress after strain exceeding yield point under tensile loading, which indicates a typical brittle behavior [46]. This phenomenon is also reflected in our stress-strain curves in Fig. 2(a). In terms of the curves of homogeneous MGs, an explicit inflection point appeared in the process of stress drop. Once the strain is beyond the inflection point, the downward trend of stress becomes gentle. This indicates that the bearing capacity of homogeneous MGs for stress reaches a critical point, and a single shear band (SB) is formed and propagates along localized region. However, there is no uniform standard to quantify the brittle or ductile behaviors at the microscale. For a macro sample, the magnitude of strain corresponding to the fracture (0 MPa) is the parameter used to distinguish ductility from brittleness. Unlike macro materials, the stress in micro materials is difficult to drop to 0 MPa, especially in the case of simulations. Interestingly, in ductile material, the stress drop from the ultimate tensile strength (σ_u) to the inflection point (σ_i) is small and smooth at the microscale. Therefore, Peng et al. [38] proposed a method to quantify the plasticity behavior of MGs based on the stress drops ($\Delta\sigma$). This method is to normalize $\Delta\sigma$ with σ_u, i.e., $\Delta\sigma/\sigma_u$. A higher normalized stress drop generally corresponds to higher propensity of deformation localization. Based on this method, the $\Delta\sigma/\sigma_u$ values of homogeneous MGs are calculated and displayed in Fig. 2 (b). It can be found that the $\Delta\sigma/\sigma_u$ values of homogeneous MGs are all greater than 2.6, so that the MG samples with $\Delta\sigma/\sigma_u$ ratio higher than 2.6 would present brittle manner. However, it should be pointed out that the value of $\Delta\sigma$ has slight errors because there is an artificial selection flexibility in the inflection point (σ_i) to some extent. Therefore, the method of $\Delta\sigma/\sigma_u$ can only empirically estimate ductility based on the stress-strain curves. In the next section, we will use another accurate method to quantify the ductility of PGMGs in detail.

Fig. 2(c, d) show the stress-strain curves of the PGMGs. According to the curves, the $\Delta\sigma/\sigma_u$ values of PGMGs are significantly lower than those of homogeneous MGs, which indicates an increase in the ductility of MGs by the phase gradients. In addition, the strains ($\sim$ 12%) corresponding to the inflection points of the PGMGs are generally larger than those of the homogeneous MGs, which means that the generation and propagation of the critical SBs are delayed. For the continuous PGMGs (A1 and B1), their ultimate tensile strengths (UTSs) naturally lie between the 2.621 GPa ($Cu_{20}Zr_{80}$) and 3.155 GPa ($Cu_{80}Zr_{20}$). However, there is an encouraging point that the UTSs of the continuous PGMGs are all significantly higher than that of the $Cu_{50}Zr_{50}$. Theoretically, the continuous PGMGs are roughly the same as the $Cu_{50}Zr_{50}$ in terms of chemical component, i.e., Cu:Zr=1:1. Thus, applying the phase gradient structure also improves the strengths of homogeneous MG counterparts. The phase gradient architectures simultaneously enhance and synergize the strength and ductility of the MGs.

Before analyzing the causes of the high strength of PGMGs, it is first necessary to understand the factors that determine the strength of homogeneous MGs. Fig. 3 presents the UTSs of homogeneous MGs as a function of Zr fraction. Clearly, the UTSs show an exponential decline as the fraction of Zr linearly increases. This result matches well with the result of Cheng et al. [45]. The declining trend of UTS basically conforms to an empirical equation:

$$\sigma_u = A * \exp\left(\frac{-x}{t}\right) + B \tag{1}$$
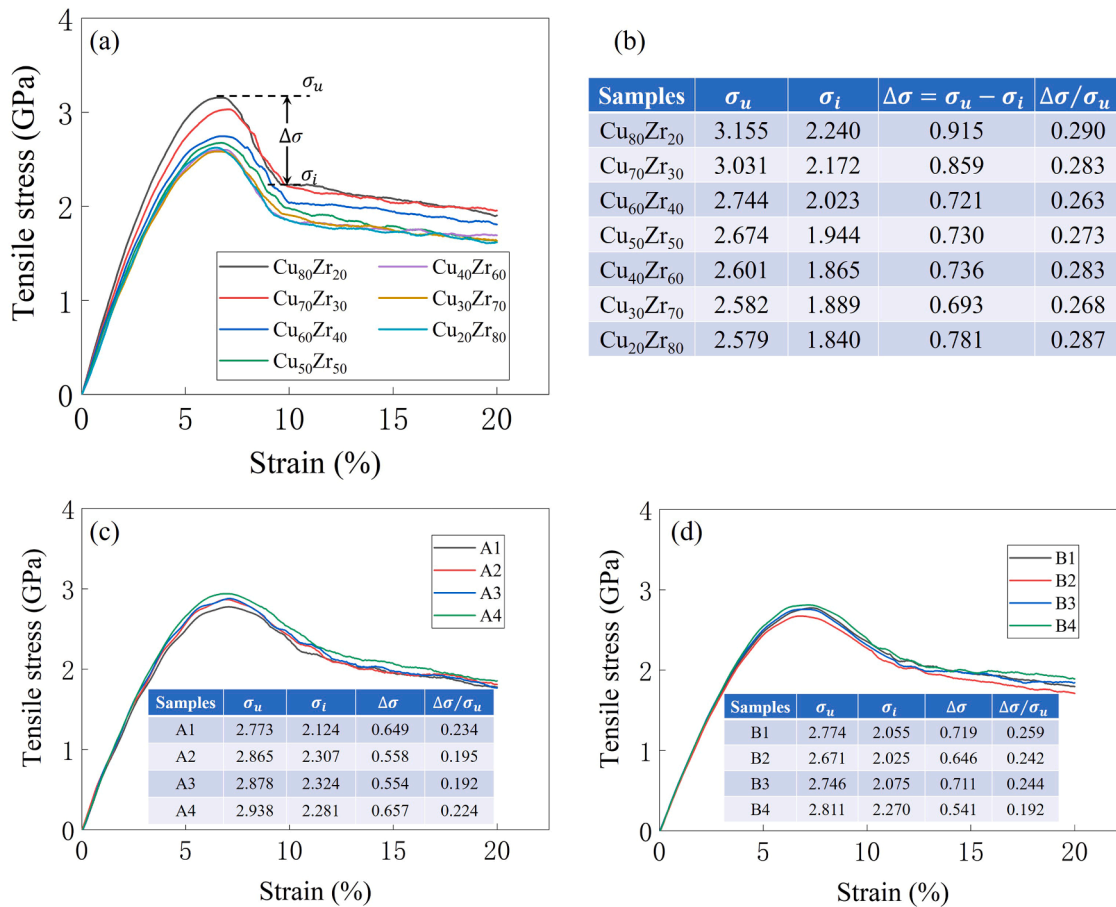
Fig. 2. Mechanical properties. (a) Stress-strain curves of the homogeneous MGs with varied compositions. (b) Stress and related parameters to indicate the plastic capacity of these homogeneous MGs in (a). (c) Stress-strain curves of A-PGMGs. (d) Stress-strain curves of B-PGMGs. Similar mechanical parameters to to (b) of PGMGs are further shown as insets of (c) and (d).
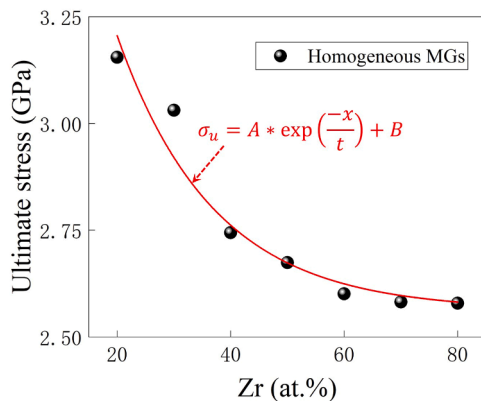

Fig. 3. The ultimate tensile strengths (UTSs) of the homogeneous MGs as a function of the fraction of Zr. The red curve is the guide line fitted to the downtrend of UTSs.

where x denotes the fraction of Zr, the A, B, and t are the fitting constants. According to dimensional analysis, t is a dimensionless coefficient of the Zr fraction, A is an attenuation coefficient whose unit is GPa. B denotes the lower limit of the UTSs of homogeneous MGs. The curve fit yields $A = 2.07 \pm 0.08$, $B = 2.56 \pm 0.06$, and $t = 17.07 \pm 1.65$. It is well known that the strength of a sample is essentially controlled by its chemical component and structure. Here, the chemical elements of homogeneous MGs are Cu and Zr. The elemental ratio of Cu and Zr

naturally affects the strength. For the chemical structures, the homogeneous MGs are long-range disorder but short-range order. Therefore, in the next part of this section, a detailed discussion of another reason for the exponential decline of UTSs in homogeneous MGs will be devoted to chemical short-range order, i.e., atomic Voronoi polyhedral (VP) clusters [47].

In terms of the chemical short-range order of MGs, atoms exhibit many analogous stacking modes by the Voronoi tessellation method. These stacking modes are named atomic VP clusters and can be characterized by the Voronoi index $<n_3, n_4, n_5, n_6>$, where n_i represents the number of i-bonded atoms on clusters [47]. Research by Mauro et al. [48] revealed that the perfect icosahedron ($<0,0,12,0>$ cluster) is a key microstructural feature in MGs. Besides, the content of this cluster significantly affects the elastic limit and yield strength. Feng et al. [47] also found that the $<0,0,12,0>$ cluster is the main building block to resist plastic deformation behavior. In our previous study [49], we revealed that the structures of three types of clusters ($<0,2,8,2>$, $<0,1, 10,2>$, and $<0,2,8,1>$) are very similar to the $<0,0,12,0>$ cluster. The three types of clusters can be transformed from the simplest structure transformations of the $<0,0,12,0>$ cluster, so they are called icosahedron-like clusters.

Fig. 4 shows the fraction of centered atoms for various atomic VP clusters in the homogeneous MGs. There is no doubt that the $<0,0,12,0>$ cluster dominates the CuZr-based amorphous structure. In addition, its number presents a decreasing trend with the fraction of Zr, similar to the law of UTSs. This result further proves the correlation between $<0,0,12,0>$ cluster and strength in amorphous structures. For the icosahedron-like clusters, the $<0,1,10,2>$ cluster basically shows a
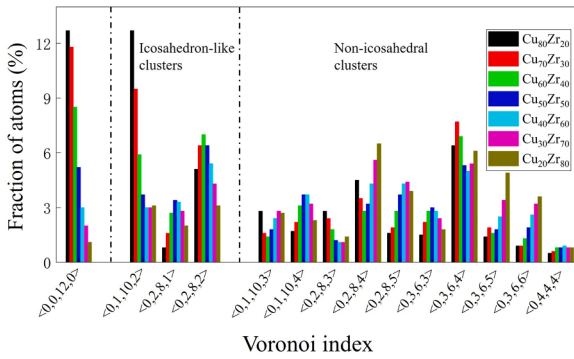
Fig. 4. Break down of the concentrations of the major VP clusters in the homogeneous MGs. Left: the perfect icosahedral clusters. Middle: the icosahedron-like clusters. Right: non-icosahedral clusters.

downward trend as the fraction of Zr increases. The $<0,2,8,1>$ and $<0,2,8,2>$ clusters first increase, and then decrease. In terms of the non-icosahedral clusters, most clusters show irregular fluctuations with the increase of the fraction of Zr. Clearly, with the exception of $<0,0,12,0>$ cluster, the number of each cluster does not show any regularity that can be correlated with the strength.

To better understand the relationship between the chemical short-range order and strength, all clusters are divided into three major types, including perfect icosahedral, icosahedron-like, and non-icosahedral clusters, respectively. Then, the clusters are summed according to their respective types. Fig. 5 displays the fractions of the three major types of atomic clusters in various homogeneous MGs. Obviously, the fractions of perfect icosahedral clusters decrease exponentially with the increase of Zr content. For the icosahedron-like clusters, their fractions decrease linearly as the content of Zr increases. However, the fractions of non-icosahedral clusters have an exponential upward trend with the content of Zr. Moreover, we have found in a previous study that the number of perfect icosahedral and icosahedron-like clusters in the plastically deformed region decreases significantly, while that of non-icosahedral clusters only fluctuates slightly [50]. Therefore, both the perfect icosahedral and icosahedron-like clusters are the main building blocks that resist the plastic deformation of MGs. Theoretically, a higher proportion of these clusters makes it more difficult for the matrix to undergo plastic deformation, resulting in a high UTS. The strength of CuZr-based MGs is directly proportional to the number of the perfect icosahedral and icosahedron-like clusters, but inversely proportional to that of the non-icosahedral clusters.

Fig. 6 shows the detailed visualization of atomic configurations in the PGMGs before deformation. It is evident that there is a big difference in the Voronoi atomic volume of local regions with different phases. Both the Cu and Zr atoms have significantly larger Voronoi volumes in regions with higher Zr content. In Fig. 6 (c, f), the Voronoi atomic
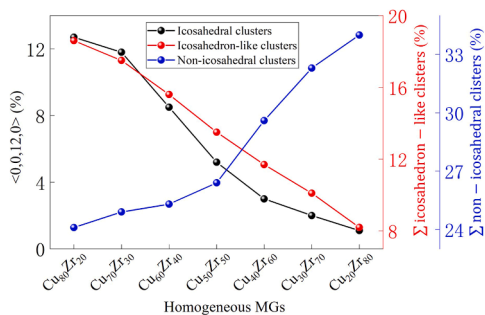
volume of continuous PGMGs (A1 and B1) increases linearly with the increase in the fraction of Zr, regardless of whether they are Cu or Zr atoms. Therefore, the content of atoms is significantly higher in the Cu-rich regions than that in the Zr-rich regions. As it is known, the gradient microstructure makes each phase have approximately the same size in PGMGs. Moreover, as mentioned in Fig. 5, the fraction of icosahedral clusters decreases exponentially with the linear increase of Zr, while that of non-icosahedral clusters shows an exponential rise. As a result, the Cu-rich regions can bring more icosahedral and icosahedron-like clusters than expected, while the Zr-rich regions possess fewer non-icosahedral clusters than expected. In other words, the phase gradient structures significantly optimize the overall atomic structure topologies of the amorphous matrixes. Therefore, we speculate that for the same chemical components, the PGMGs should possess more icosahedral and icosahedron-like clusters and fewer non-icosahedral clusters than the homogeneous MGs.

Here, we need a structural parameter to prove the above speculation about the features of the atomic structure topologies in PGMGs. Fortunately, these features can be characterized by the local five-fold symmetry (LFFS) of atoms. LFFS denotes the percentage of pentagons in each cluster and plays an essential role in the inherent characteristic of the microstructure of MGs [19,51–53], which is defined as:

$$f_i^5 = \frac{n_i^5}{\sum_{k=3,4,5,6} n_i^k} \tag{2}$$

where $n_i^k (k= 3,4,5,6)$ means the number of k-edge polygons in the polyhedron i. Moreover, to reflect the average degree of LFFS in the matrixes of MGs, an overall structural parameter W is defined as:

$$W = \sum_i \left(f_i^5 \times P_i \right) \tag{3}$$

herein P_i is the fraction of type-i clusters in all clusters. Clearly, the f_i^5 values of the central atoms of icosahedral and icosahedron-like clusters are significantly higher than those of non-icosahedral clusters. Thus, a higher value of W indicates that this matrix of MG possesses more icosahedral and icosahedron-like clusters. On the right side of Fig. 6(a, d), the atoms with higher LFFS in the continuous PGMGs show an intimate gathering in the Cu-rich regions and a substantial decrease in the direction of decreasing Zr.

As mentioned above, the chemical components (elemental ratios) of MGs make a difference in their strengths as well. Therefore, the comparison object of each PGMG is a homogeneous MG with the same chemical component. Based on the chemical component analysis of PGMGs, the Cu fractions of A1, A2, A3, and A4 are 52%, 59.1%, 60.5%, and 62.1%, respectively, and those of B1, B2, B3, and B4 are 51%, 45.2%, 46.9%, and 48.8%, respectively. Here, the homogeneous MGs with the same chemical components as PGMGs are constructed. In Fig. 7 (a), the W values of PGMGs are indeed higher than those of homogeneous MGs under the same chemical components, which shows that our speculation is entirely correct. Moreover, Fig. 7(b) also proves that the matrixes of PGMGs have higher UTSs than those of homogeneous MGs due to the higher number of icosahedral and icosahedron-like clusters.

3.2. Plastic deformation behavior

To comprehensively realize the plastic behavior of the PGMGs, the deformation and failure are characterized by calculating the von Mises shear strain of each atom (η_i^{Mises}) [54]. For the calculation of η_i^{Mises}, two configurations (reference and current) are required. It should be pointed out that to study the atomic movement and rearrangement in detail, the reference configuration is not set in stone.

It was mentioned earlier that the PGMGs have a similar chemical component to $Cu_{50}Zr_{50}$ homogeneous MG. Therefore, we also analyzed the von Mises shear deformation of $Cu_{50}Zr_{50}$ homogeneous MG. Fig. 8
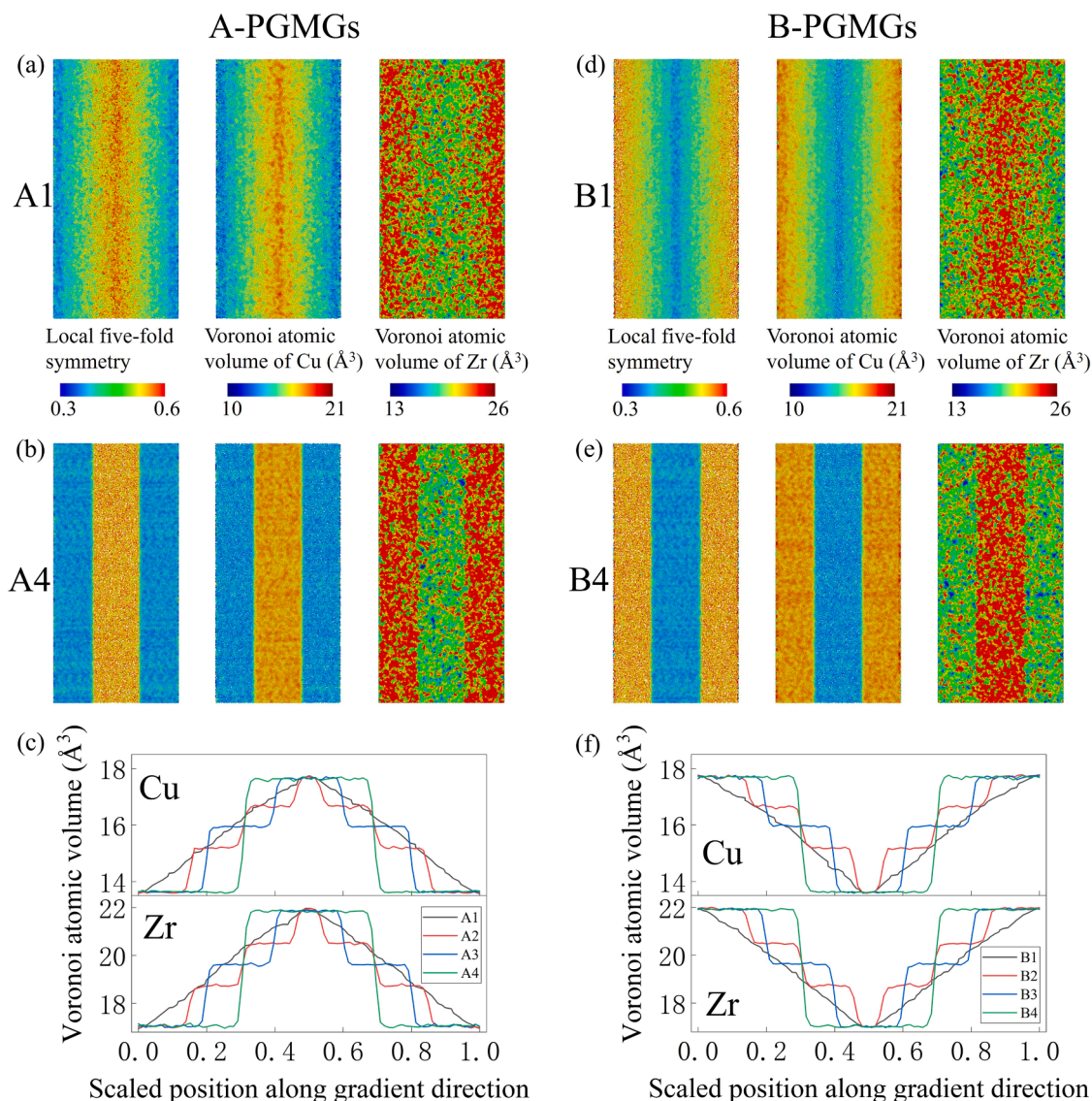

Fig. 5. The fraction of three major types of atomic clusters in various homogeneous MGs. The three major types of atomic clusters are perfect icosahedral, icosahedron-like, and non-icosahedral clusters, respectively.

Fig. 6. The structural features of PGMGs. The local five-fold symmetry, and Voronoi volumes of constituent atoms in (a) A1 and (b) A4 glasses as illustrated in Fig. 1. (c) Coarse-grained Voronoi volume along the gradient direction for A1-A4 samples. (d)-(f) The same plots to (a)-(c) for the B1-B4 gradient samples.

illustrates the local deformation evolution during tensile loading in the A-PGMGs, homogeneous MG, and B-PGMGs. For the homogeneous $Cu_{50}Zr_{50}$ MG, a single critical SB is generated after the strain of 10% and leads to sample failure. This feature is consistent with the previous result [46]. However, for the A-PGMGs, the failure is co-driven by multiple critical SBs. In terms of the continuous PGMG (A1), at $\varepsilon = 8\%$, initial SB is first triggered at the center, as displayed in Fig. 8(a). This result indicates that the initial SB of PGMGs may tend to nucleate around Zr-rich regions. Beyond $\varepsilon = 8\%$, the initial SB propagates to the free surfaces of the sample by maximally resolved shear stress oriented at ~45° to the elongation direction. Interestingly, the initial SB diffuses and branches as it propagates, contrary to the single SB in homogeneous MGs. Based on the above results, we consider that there should be an increasing resistance to SBs' propagation for continuous PGMG. Thus, the initial SB generates branches in the two directions of maximally resolved shear stress. Here, the two branches of the initial SB are defined as ①, and ②, respectively. In Fig. 8(a), at $\varepsilon = 20\%$, the SB ① has a spatial step as the action of the SB ②, which indicates that both SB ① and ② are constantly undergoing plastic deformation. As multiple SBs jointly drive plastic deformation, the generation of critical SBs is delayed, resulting in the postponement of failure. For the stepped PGMGs (A2, A3, and A4), at the

embryonic stage of deformation, several SBs are nucleated, unlike the single initial SB in the continuous PGMG. This result reveals that the propagation resistance of SBs is stronger in stepped PGMGs than that in continuous PGMG. Moreover, these SBs interact with each other during propagation and appear diffusion and branches, indicating the delocalization mechanism of plastic deformation and the improvement of ductility [41]. However, it can be noticed that although A4 has a large number of SBs, they exhibit a concentration in the middle of the matrix, resulting in the necking of the system. Therefore, we speculate that the ductility of A4 may be weaker than that of A3.

Clearly, the failure of B-PGMGs is also driven by multiple critical SBs. In terms of B1 (continuous PGMG), at $\varepsilon = 14\%$, a clear critical SB has been formed in the system, as shown in Fig. 8(f). However, one can note from this snapshot that there is a growing SB above the critical one. When the strain increases to 20%, a critical SB with thick of 15.3 nm is generated in the system. This thick critical SB is formed by merging several SBs, so it also delocalizes plastic deformation. For the stepped PGMGs (B2, B3, and B4), multiple SBs nucleate and propagate in the system. As the stepped amplitude of phase gradient increases, the number of SBs increases to delocalize plastic deformation, resulting in the improvement of ductility. Moreover, the distribution of SBs in the B-
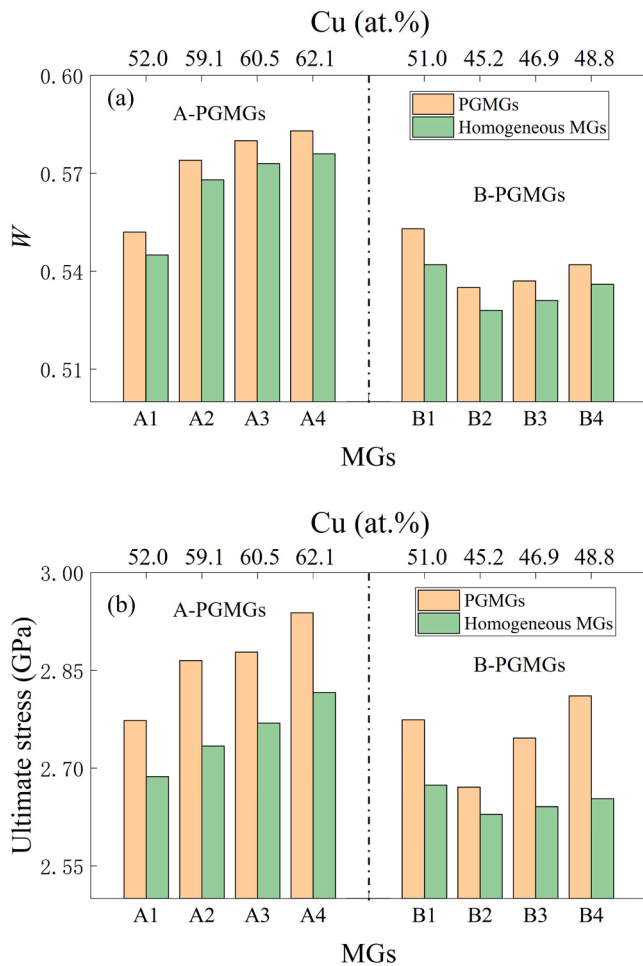
Fig. 7. (a) The overall degree of five-fold symmetry parameter in PGMGs and homogeneous MGs. (b) The UTSs in the PGMGs and homogeneous MGs. The PGMGs and homogeneous MGs have the same chemical components when they are compared. The fractions of Cu in A1, A2, A3, and A4 are 52%, 59.1%, 60.5%, and 62.1%, respectively. While in B1, B2, B3, and B4, they are 51%, 45.2%, 46.9%, and 48.8%, respectively.

PGMGs is relatively uniform. Therefore, we consider that the ductility of B-PGMGs increases with the stepped amplitude of the phase gradient, at least at the present studied length scale.

Fig. 9 displays the distribution of local atomic shear strain along the gradient direction during deformation in the PGMGs. Clearly, high η_i^{Mises} mainly concentrates in the middle of A-PGMGs, while that appears on the outer surfaces of B-PGMGs. Correspondingly, at $\varepsilon = 10\%$, the density of the shear transformation zones (STZs) of A-PGMGs along the Y-direction in the core is higher, whereas that of B-PGMGs on the free surfaces is higher, as presented in Fig. 8. In light of these results about the density of STZs, it can be concluded that the initial SB of PGMGs tends to nucleate around Zr-rich regions. Therefore, there is only one nucleation region (middle of the sample) for the SBs of A-PGMGs. However, the B-PGMGs have two regions (outer surfaces of the system) for the nucleation of SBs. As a result, the nucleation sites of SBs in B-PGMGs have higher uncertainty than those in A-PGMGs. That is to say, the probability of concentrated SBs occurred in B-PGMGs is lower than that in A-PGMGs. In this way, we can explain why the A4 sample shows a concentration of SBs while the B-PGMGs display uniform distribution.

The atoms in Zr-rich regions exhibiting higher atomic strain deserve further investigation. In terms of MGs, the atomic strain is mainly controlled by the dynamic competition between the annihilation and generation of free volume [55]. A higher free volume also makes an

atom more likely to undergo plastic deformation [56]. Besides, as shown in Fig. 5, there are huge differences in the atomic chemical short-range order of the MGs in each phase. Therefore, the relationship between atomic chemical short-range order and free volume requires in-depth analysis. To detailedly analyze the influence of chemical short-range order (VP clusters) on free volume, studying the atomic-packing efficiency (APE), one key parameter of VP clusters, is necessary. The equation of APE was proposed by Yang et al. [57] to describe the space utilization of VP clusters:

$$\eta = \frac{1}{n} \sum_{i=1}^{n} \frac{V_{ia}}{V_{iu}} \tag{4}$$

where n is the total number of a certain type of VP clusters. Here, Fig. 10 shows the calculation of APE in detail through the three-dimensional atomic configuration diagram of <0,0,12,0> cluster. V_{iu} represents the volume of the i-th cluster itself. For the <0,0,12,0> cluster, V_{iu} is the total volume of the yellow area in Fig. 10(b). V_{ia} denotes the volume of the embedded atoms inside the i-th cluster. To facilitate the calculation, the i-th cluster is first divided into several tetrahedra, as displayed in Fig. 10(c). Then, the embedded atomic volume in all tetrahedra is summed to gain V_{ia}. Based on the above definition, a high-value η indicates that this VP cluster has a lower free volume and better space utilization.

Table 1 presents the APEs of icosahedral, icosahedron-like, and non-icosahedral clusters in different homogeneous MGs. To establish a comparison, Table 1 also includes the average APEs for Cu-centered or Zr-centered clusters. It is apparent that in homogeneous MGs, regardless of whether the clusters are Cu-centered or Zr-centered, the APEs of <0,0,12,0> clusters are the highest in all clusters. Moreover, clusters with an icosahedron-like structure have a close APE to <0,0,12,0> clusters, suggesting further that microstructurally, icosahedron-like clusters are indeed similar to clusters like <0,0,12,0> clusters. For the non-icosahedral clusters, their APEs are significantly lower than the icosahedral and icosahedron-like clusters. As a result, the average APEs (Cu-centered or Zr-centered clusters) naturally lie between the icosahedral and non-icosahedral clusters. Moreover, a higher fraction of <0,0,12,0> and icosahedron-like clusters signals that this MG has lower free volume and better space utilization. Correspondingly, the high fraction of non-icosahedral clusters leads to low space utilization and high free volume in MG.

Fig. 11 presents the APEs of three major types of clusters as a function of the fraction of Zr. Here, the APEs of all clusters in the true sense are also calculated as yellow scatters. Clearly, in a nearly linear way, the APEs of the icosahedral and icosahedron-like clusters decrease as the fraction of Zr increases for both Cu-centered and Zr-centered clusters. Therefore, the increase of the content of Zr not only reduces the fraction of icosahedral and icosahedron-like clusters but also decreases the APEs of these clusters. For the non-icosahedral clusters, their APEs do not show significant changes with the content of Zr. These phenomena indicate that although increasing the fraction of Zr increases the number of non-icosahedral clusters, it does not affect the APEs of these clusters. Thus, there are two main reasons for the lower APEs in Zr-rich homogeneous MGs. On the one hand, the Zr-rich homogeneous MGs have a lower fraction of the icosahedral and icosahedron-like clusters and a higher content of the non-icosahedral clusters. On the other hand, the APEs of the icosahedral and icosahedron-like clusters of Zr-rich homogeneous MGs are already at a relatively low level. Finally, based on the yellow scatters in Fig. 11, the APEs of homogeneous MGs show a linearly decreasing trend as the fraction of Zr increases:

$$\eta_{MGs} = 0.7214 - 0.087x \tag{5}$$

where x represents the fraction of Zr. This indicates that the free volume of the CuZr-based MGs increases with the fraction of Zr. It is worth noting that there is a limitation to the Eq. (5) which holds only if x lies between 20 and 80. Therefore, the 0.7214 only represents the ideal
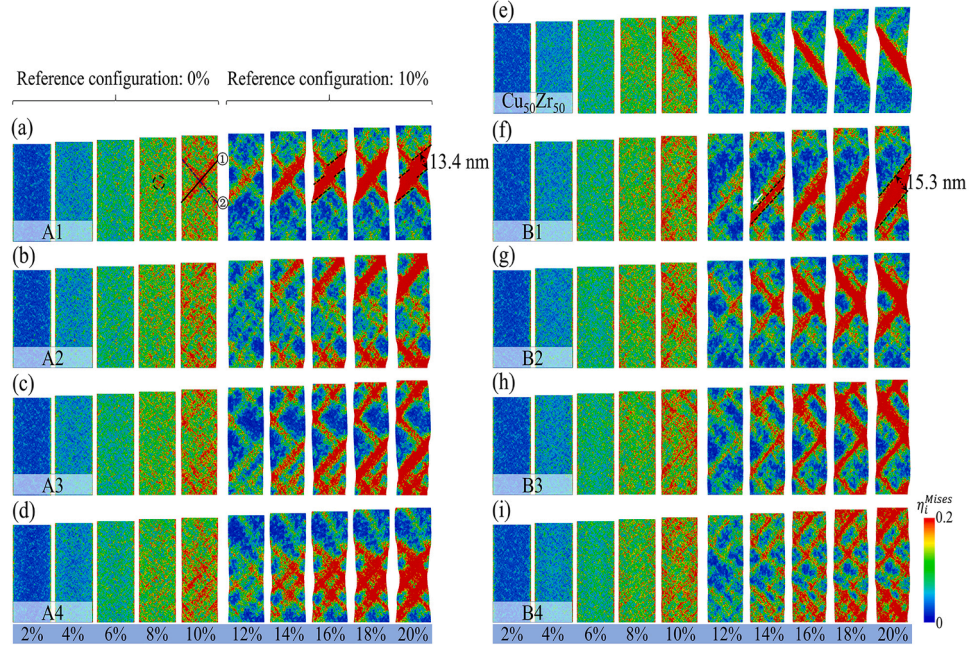
Fig. 8. Visualization of local deformation in the A-PGMGs, homogeneous MG, and B-PGMGs. The von Mises shear strain η_i^{Mises} are shown at different magnitudes of strain. When strain is below 10%, the reference configuration is undeformed sample. The reference configuration for strain above 10% is set to that deformation at 10% shear. (a) A1. (b) A2. (c) A3. (d) A4. (e) Cu$_{50}$Zr$_{50}$. (f) B1. (g) B2. (h) B3. (i) B4.
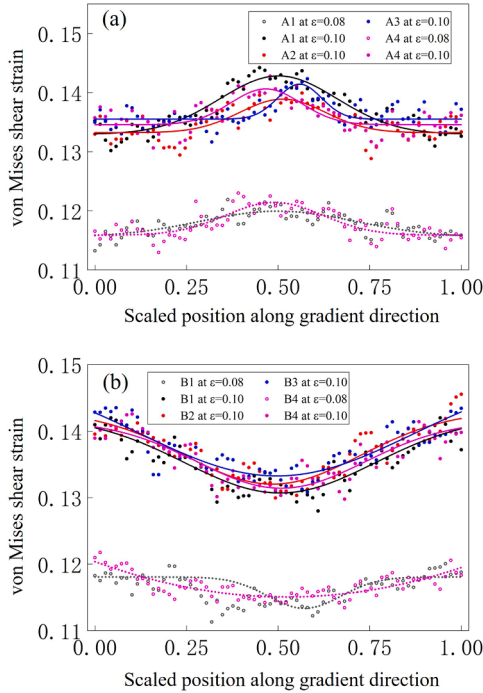

Fig. 9. Distribution of local atomic shear strain along the gradient direction during deformation in the PGMGs. The open dots represent a strain of 0.08, and the filled dots denote a strain of 0.10. Different colors represent different samples. The curves are served as a guide to the eye. (a) A-PGMGs. (b) B-PGMGs.

maximum of the APE for homogeneous MGs, not the real APE of single-element amorphous Cu. 0.087 is the linear attenuation coefficient of APE corresponding to the fraction of Zr. In the amorphous alloy, the free volume (V_f) is defined as the current average atomic volume minus the average atomic volume in the ideally ordered structure [58].
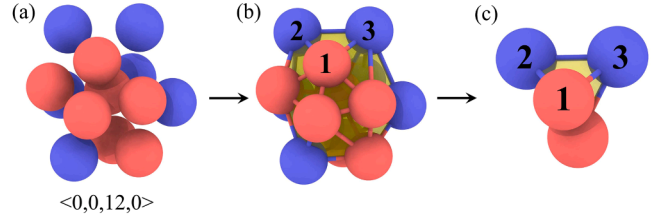

Fig. 10. (a) A perfect icosahedral cluster in the Cu$_{50}$Zr$_{50}$. (b) Ideal atomic arrangement in <0,0,12,0> Voronoi tessellation. (c) One of its tetrahedron components. Atoms with numbers are shell atoms in the tetrahedron component. The blue and red balls stand for Zr and Cu atoms, respectively.

Additionally, to simplify the calculations, the free volume of an amorphous alloy is usually reduced. The reduced free volume is calculated as [59,60]:

$$\overline{V}_f = \frac{V_c - V_i}{V_i} \tag{6}$$

where V_c is the volume of the amorphous alloy, V_i denotes the volume of the ideally ordered structure with the same chemical components. Here, the atomic volumes of Cu and Zr are Ω_{Cu} and Ω_{Zr}, respectively. Thus, the volumes of the Cu and Zr monocrystals are defined as:

$$\begin{cases} V_{Zr} = \dfrac{M \cdot \Omega_{Zr}}{\eta_{Zr}} \\[2mm] V_{Cu} = \dfrac{\left(\dfrac{1-x}{x}\right) \cdot M \cdot \Omega_{Cu}}{\eta_{Cu}} \\[2mm] V_i = V_{Zr} + V_{Cu} \\[2mm] V_c = \dfrac{M \cdot \Omega_{Zr} + \left(\dfrac{1-x}{x}\right) \cdot M \cdot \Omega_{Cu}}{\eta_{MGs}} \end{cases} \tag{7}$$

where x is the fraction of Zr, M denotes the number of Zr atoms, η_{Zr} and η_{Cu} are the APEs of the Zr and Cu monocrystals. $\overline{V}_f$ can be calculated by

Table 1

The atomic-packing efficiency (APE) of <0,0,12,0>, icosahedron-like, and non-icosahedral clusters in different homogeneous MGs. The average APEs for Cu-centered or Zr-centered clusters are also listed.

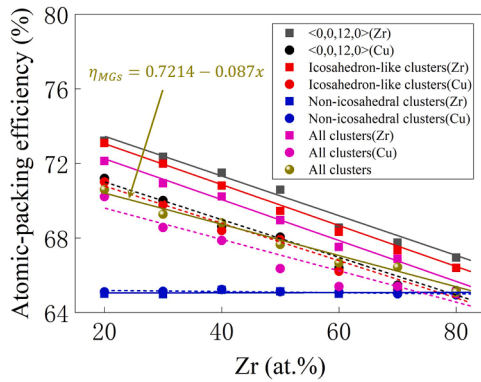| Sample	Clusters	Atomic-packing efficiency (%)	
		Zr-centered	Cu-centered
$Cu_{80}Zr_{20}$	<0,0,12,0>	73.2115	71.1923
	Icosahedron-like clusters	73.0913	71.0041
	Non-icosahedral clusters	64.9971	65.1123
	All clusters	72.1298	70.2163
$Cu_{70}Zr_{30}$	<0,0,12,0>	72.3462	70.0048
	Icosahedron-like clusters	71.9856	69.7798
	Non-icosahedral clusters	64.9798	65.1314
	All clusters	70.9279	68.5633
$Cu_{60}Zr_{40}$	<0,0,12,0>	71.4952	68.6202
	Icosahedron-like clusters	70.8077	68.3865
	Non-icosahedral clusters	65.2113	65.2354
	All clusters	70.2212	67.8655
$Cu_{50}Zr_{50}$	<0,0,12,0>	70.5817	68.0433
	Icosahedron-like clusters	69.4375	67.9103
	Non-icosahedral clusters	65.1345	65.1187
	All clusters	68.9519	66.3525
$Cu_{40}Zr_{60}$	<0,0,12,0>	68.5481	66.3846
	Icosahedron-like clusters	68.3202	66.2144
	Non-icosahedral clusters	64.9987	65.0932
	All clusters	67.5125	65.3895
$Cu_{30}Zr_{70}$	<0,0,12,0>	67.7452	65.4615
	Icosahedron-like clusters	67.3365	65.2184
	Non-icosahedral clusters	65.1265	64.9987
	All clusters	66.8768	65.3984
$Cu_{20}Zr_{80}$	<0,0,12,0>	66.9375	65.1740
	Icosahedron-like clusters	66.3846	65.0753
	Non-icosahedral clusters	65.0186	64.9512
	All clusters	65.1143	65.0131

Fig. 11. The atomic-packing efficiency of various types of clusters as a function of Zr fraction. Different colors indicate different types of atomic clusters. For the same cluster type, different central atoms are distinguished by different dot shapes. The lines represent apparent linear fits.

substituting Eq. (7) into (6). It is worth noting that the atomic structures of Cu and Zr single crystals are FCC (face-centered cubic) and HCP (hexagonal close-packed), respectively. Therefore, the η_{Cu} is equal to 0.74. Moreover, the η_{Zr} with an ideally HCP structure is approximately equal to 0.74. Here, we assume that $\eta_{Zr} \approx \eta_{Cu} = 0.74$, so the reduced free volume of the CuZr-based MGs can be simplified as:

$$\overline{V}_f \approx \frac{\eta_{Zr}}{\eta_{MGs}} - 1 = \frac{0.74}{0.7214 - 0.087x} - 1 \qquad (8)$$

In light of Eq. (8), with increasing content of Zr in the CuZr-based MGs, the reduced free volume increases. As a result, it can be concluded that the phase gradient structures result in an inhomogeneous free volume distribution in MGs. For the homogeneous MGs, the initial SB develops spontaneously by the autocatalytic STZs of successive strain and rotation fields [61]. In other words, after the local nucleation of the

initial SB, STZs spontaneously accumulate around it by means of rotational percolation during successive strain, leading to the formation of a critical SB. However, in a study of MG with heterogeneous free volume, Şopu et al. [62] found that the rotational percolation of STZs is altered at the interface, leading to the obstruction of the autocatalytic activation mechanism of STZs. Therefore, for the continuous PGMGs, the rotational percolation of STZs is continuously changing during successive strain, indicating the failure of the autocatalytic activation mechanism of STZs. The initial SB has an increasing resistance during the propagation along one direction. As a result, the initial SB branches in two directions of the maximally resolved shear stress, contrary to the homogeneous MGs. For the stepped PGMGs, the difference in free volume is more significant at interfaces, resulting in more excellent resistance to the propagation of SBs. Therefore, the systems tend to generate several SBs in regions with higher free volume (Zr-rich regions). Moreover, as the step amplitude increases, more SBs appear in the stepped PGMGs.

Currently, with advances in experimental techniques, Tang et al. [63] fabricated two different types of gradient MGs with spatially gradient distributed free volume contents. They also found that the free volume gradient enhanced the ductility of MGs. Such enhanced plasticity results from the shear deformation deflection due to free volume mismatch. The shear deformation deflection fundamentally suppresses the unlimited shear localization on a straight plane that would be expected in homogeneous MGs. These experimental phenomena prove the change in the rotational percolation of STZs caused by the free volume mismatch of MGs, which makes the autocatalytic activation mechanism ineffective. Their experimental results further support the reliability of the ductility improvement of PGMGs given by the simulation results.

Although we have completed mechanistic studies on the enhancement of ductility in PGMGs, the degree of the enhancement of each PGMG is still elusive. To accurately quantify the ductility of PGMGs, Fig. 12 shows another micro method without artificial error, i.e., the inhomogeneity parameter h [64]. This method calculates the degree of inhomogeneity of the spatial distribution of atoms undergoing plastic deformation. Here, based on Fig. 8, atoms with an η_i^{Mises} value exceeding 0.2 are considered to those have undergone plastic deformation. The value of h is calculated according to Eq. (9):

$$h = \frac{1}{2N} \sum_{k=1}^{r} \left(8.89^{1-k} \sum_{i=1}^{2^{3k}} |m_i - \overline{m}(2^{3k})| \right) \qquad (9)$$

The detailed explanation and usage of the Eq. (9) can be found in Ref. [64]. The value range of h is [0,1]. A high value of h indicates the inhomogeneous spatial distribution of atoms, while a low value denotes a uniform spatial distribution. Thus, a higher h indicates a lower degree of delocalization of SBs, which implies a lower ductility. At the early stage, the deformation behavior transitions from uniform deformation to localized SBs, so h increases with increasing strain, as displayed in Fig. 12(a, c). The instant ductility of each PGMG cannot be compared by the values of h at this stage. In Fig. 12(b, d), at the propagation stage of SBs, the h values of PGMGs under the same strain follow the relationship as: $h_{A1} > h_{A2} > h_{A3} < h_{A4}$, $h_{B1} > h_{B2} > h_{B3} > h_{B4}$. According to these results, the ductility of A-PGMGs first increases and then decreases as the stepped amplitude increases, while that of B-PGMGs always increases. Finally, one can also note from the Fig. 12(b, d) that the h values of some samples (A3, B3, and B4) decrease slightly as the strain increases. For these samples, there are multiple evenly distributed critical SBs, as presented in Fig. 8. As strain proceeds, the multiple critical SBs become evenly distributed and collectively contribute to failure, resulting in progressively more homogeneous plastic deformation.

Fig. 13 displays the UTS and spatial distribution h as functions of stepped amplitude in PGMGs. Here, the selected values of h correspond to the strain of 20%. For the A-PGMGs, the UTS increases monotonically with the stepped amplitude, whereas the h fluctuates. For the B-PGMGs, the h decreases monotonically as the stepped amplitude increases, while the UTS fluctuates. As a result, the A-PGMGs are more appropriate for
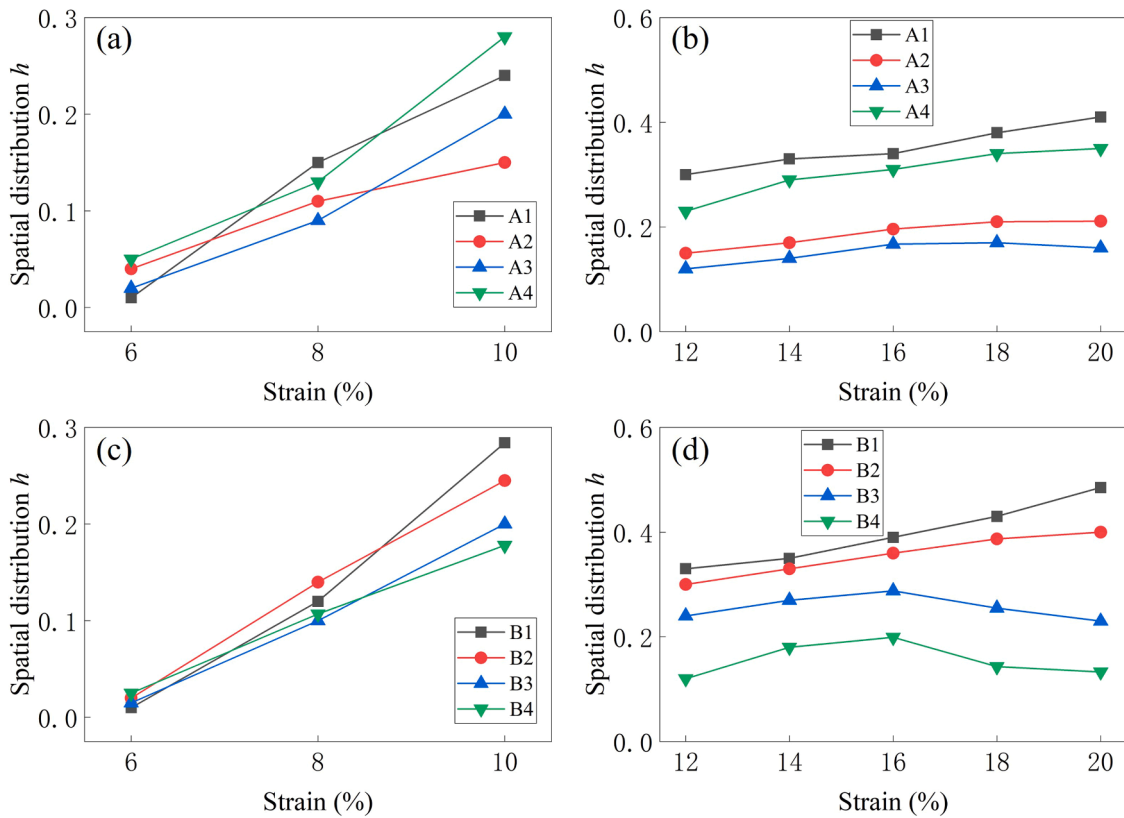
Fig. 12. Inhomogeneity parameter h of the atoms with η_i^{Mises} higher than 0.2 as functions of strain. (a)-(b) for A-PGMGs, and (c)-(d) for B-PGMGs. Left column with reference to the undeformed samples, and right column with reference to the sample deformation at shear strain of 10%; see Fig. 8.
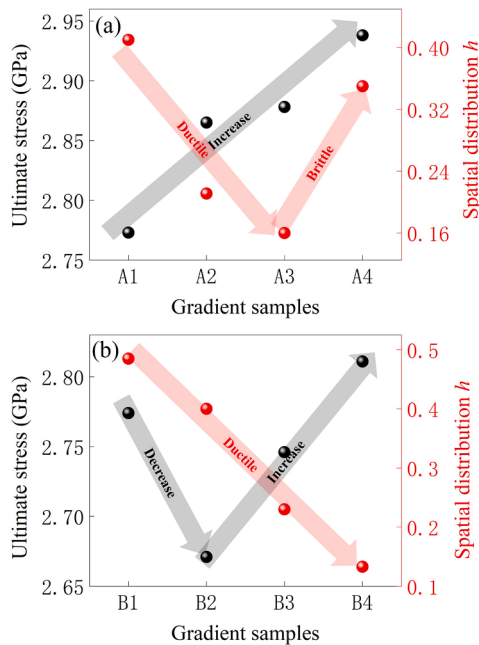

Fig. 13. The UTS and the spatial distribution h as functions of the stepped amplitude in PGMGs. The values of h are calculated when the global tensile strain is 20%. (a) A-PGMGs. (b) B-PGMGs.

strength-focused applications, whereas the B-PGMGs are better suited for ductility-focused scenarios. In other words, the strategy of PGMGs not only improves strength and ductility simultaneously but also tailors the mechanical synergy for various application circumstances.

3.3. Experimental synthesis of PGMGs

At present, there are still many technical difficulties in the experimental synthesis of such PGMGs. Here, we only provide four possible synthetic paths. I) MG slices with different phases can be generated by melt spinning or hot pressing [65,66]. Then, a PGMG is generated by second annealing around glass transition temperature of a combination of different MGs arranged in a gradient range of phases. II) PGMGs can also be synthesized through the concept of cold-joining via ultrasonic vibration [67,68]. The above MG slices are first combined by a gradient range of phases. Then, the interfaces of PGMGs realize cold-joining by long-term periodic ultrasonic vibration. III) The third alternative to generate the PGMGs is by continuously changing the phases of MGs during a periodic island-layer-island deposition [69]. But this method is limited in the fabricating large length scale samples. IV) With the development of science and technology, additive manufacturing may become the fourth possible preparation method of PGMGs [70,71]. Phase gradients can be achieved by altering the amorphous materials during the 3D printing. Among these potential methods, additive manufacturing is a relatively feasible method for PGMG preparation. Currently, many types of gradient MGs have been produced by the 3D printing. These gradient MGs have been systematically summarized and reviewed by Zhang et al. [70].

Currently, we reveal free volume gradients induced by the phase gradients in the CuZr-based MGs, which leads to the delocalization of SBs at the microscale. At the macroscopic scale, Wang et al. [40] also found the delocalization of SBs by finite element simulation of free volume gradients. This indicates that our simulation results are reasonable even at the macro scale. Moreover, as shown in Fig. 2(a), Young's modulus of each phase of MGs differs during tensile loading, so the phase gradient structures also lead to stress gradients inside the sample. In an experimental study, Zhao et al. [42] revealed that stress

gradients simultaneously enhance the strength and ductility of MGs. Therefore, the PGMGs, coupling free volume and stress gradients, should exhibit more excellent mechanical properties at the macroscopic scale. As the results of current work and these synthetic strategies of PGMGs, we hope that experimental work in the MG field will be stimulated.

4. Conclusions

In this work, MD simulations are employed to study the effects of the two types of phase gradient microstructure (A-PGMGs and B-PGMGs) on the mechanical properties of CuZr-based MGs, where we analyzed the ultimate tensile strengths, local atomic topology, plastic deformation behavior, and free volume. The simulations show that using phase gradient architectures, atomic structure topology of the matrixes can be optimized, i.e., for a given chemical component, the number of mechanically stable Voronoi polyhedra with icosahedral and icosahedron-like structures is higher in PGMGs than that in homogeneous MGs. These Voronoi polyhedra are the main building blocks to resist plastic deformation behavior, so the PGMGs further increase the strength.

An exciting feature of PGMGs is that the initial SB tends to nucleate around Zr-rich regions during plastic deformation. Based on this phenomenon, further studies confirm that the local free volume of PGMGs increases with the content of Zr. As a result of the higher free volume in Zr-rich regions, shear deformation will be easier. Moreover, a model based on the fraction of Zr is proposed to predict the free volume at the local level in PGMGs. Due to the local heterogeneity of free volume in PGMGs, the autocatalytic activation mechanism of STZs is invalidated during successive strain, indicating a resistance to the propagation of initial SB. As a result, not only the initial SB branches but also more SBs nucleate in Zr-rich regions. Multiplication of SBs delocalizes the plastic deformation, improving the overall ductility of the matrixes. Therefore, the strength and ductility of MGs are improved simultaneously by the phase gradient architecture.

Finally, the results also show that with the change of step amplitude, the response of strength in A-PGMGs is more significant, while that of ductility in B-PGMGs is stronger. Thus, another advantage of PGMGs is their ability to further tune the mechanical synergy of strength and ductility by selecting a different type of PGMGs and changing the stepped amplitude of phase gradients.

CRediT authorship contribution statement

Yunlong Guan: Conceptualization, Data curation, Software, Visualization, Writing – original draft, Writing – review & editing. **Yunjiang Wang:** Data curation, Validation, Writing – original draft, Writing – review & editing. **Weidong Song:** Funding acquisition, Resources, Methodology, Supervision, Writing – original draft, Writing – review & editing.

Declaration of Competing Interest

The authors declare that they have no known competing financial interests or personal relationships that could have appeared to influence the work reported in this paper.

Data Availability

No data was used for the research described in the article.

Acknowledgment

References

[1] Kosiba K, et al. Modulating heterogeneity and plasticity in bulk metallic glasses: role of interfaces on shear banding. Int J Plast 2019;119:156–70. https://doi.org/10.1016/j.ijplas.2019.03.007.
[2] Lu L, et al. Ductile fracture of bulk metallic glass $Zr_{50}Cu_{40}Al_{10}$ under high strain-rate loading. Mater Sci Eng A 2016;651:848–53. https://doi.org/10.1016/j.msea.2015.11.040.
[3] Jodar B, et al. Localized atomic segregation in the spalled area of a $Zr_{50}Cu_{40}Al_{10}$ bulk metallic glasses induced by laser-shock experiment. J Phys D Appl Phys 2018;51:065304. https://doi.org/10.1088/1361-6463/aaa322.
[4] Gan KF, et al. Elucidating how correlated operation of shear transformation zones leads to shear localization and fracture in metallic glasses: tensile tests on CuZr based metallic-glass microwires, molecular dynamics simulations, and modelling. Int J Plast 2019;119:1–20. https://doi.org/10.1016/j.ijplas.2019.02.011.
[5] Wu FF, Zheng W, Wu SD, Zhang ZF, Shen J. Shear stability of metallic glasses. Int J Plast 2011;27:560–75. https://doi.org/10.1016/j.ijplas.2010.08.004.
[6] Sha ZD, Branicio PS, Lee HP, Tay TE. Strong and ductile nanolaminate composites combining metallic glasses and nanoglasses. Int J Plast 2017;90:231–41. https://doi.org/10.1016/j.ijplas.2017.01.010.
[7] Polk DE, Turnbull D. Flow of melt and glass forms of metallic alloys. Acta Metall 1972;20:493–8. https://doi.org/10.1016/0001-6160(72)90004-1.
[8] Yoshikawa T, Tokuda M, Inaba T. Influence of thermoplastic deformation on mechanical properties of Zr-based bulk metallic glasses at room temperature. Int J Mech Sci 2008;50:888–96. https://doi.org/10.1016/j.ijmecsci.2007.09.005.
[9] Donovan PE, Stobbs WM. The structure of shear bands in metallic glasses. Acta Metall 1981;29:1419–36. https://doi.org/10.1016/0001-6160(81)90177-2.
[10] Wang J, Li R, Hua N, Zhang T. Co-based ternary bulk metallic glasses with ultrahigh strength and plasticity. J Mater Res 2011;26:2072–9. https://doi.org/10.1557/jmr.2011.187.
[11] Tao K, Qiao JC, He QF, Song KK, Yang Y. Revealing the structural heterogeneity of metallic glass: mechanical spectroscopy and nanoindentation experiments. Int J Mech Sci 2021;201:106469. https://doi.org/10.1016/j.ijmecsci.2021.106469.
[12] Xiaoqing Z, Shukui L, Liu J, Wang Y, Xing W. Self-sharpening behavior during ballistic impact of the tungsten heavy alloy rod penetrators processed by hot-hydrostatic extrusion and hot torsion. Mater Sci Eng A 2010;527:4881–6. https://doi.org/10.1016/j.msea.2010.04.050.
[13] Deb Nath SK. Thermal conductivity and mechanical properties of ZrxCu90−xAl10 under tension using molecular dynamics simulations. Int J Mech Sci 2018;144:836–41. https://doi.org/10.1016/j.ijmecsci.2017.08.037.
[14] Winkler B, et al. Dispersion relation of an OH-stretching vibration from inelastic X-Ray scattering. Phys Rev Lett 2008;101:065501. https://doi.org/10.1103/PhysRevLett.101.065501.
[15] Ramamurty U, Lee ML, Basu J, Li Y. Embrittlement of a bulk metallic glass due to low-temperature annealing. Scr Mater 2002;47:107–11. https://doi.org/10.1016/S1359-6462(02)00102-1.
[16] Narayan RL, Tandaiya P, Narasimhan R, Ramamurty U. Wallner lines, crack velocity and mechanisms of crack nucleation and growth in a brittle bulk metallic glass. Acta Mater 2014;80:407–20. https://doi.org/10.1016/j.actamat.2014.07.024.
[17] Shi Y, Falk M. Atomic-scale simulations of strain localization in three-dimensional model amorphous solids. Phys Rev B 2006;73. https://doi.org/10.1103/PhysRevB.73.214201.
[18] Li T, Shen Y, Zheng G. Characterization on the glass forming ability of metallic nano-glasses by the dynamic scaling for mechanical loss in supercooled liquid state. Scr Mater 2021;203:114109. https://doi.org/10.1016/j.scriptamat.2021.114109.
[19] Peng HL, Li MZ, Wang WH. Structural signature of plastic deformation in metallic glasses. Phys Rev Lett 2011;106:135503. https://doi.org/10.1103/PhysRevLett.106.135503.
[20] Song W, Yu Y, Guan Y. Role of void shape on shock responses of nanoporous metallic glasses via molecular dynamics simulation. Int J Mech Sci 2022;218:107076. https://doi.org/10.1016/j.ijmecsci.2022.107076.
[21] Tao K, Qiao JC, Zhang L, Pelletier JM. Dynamic mechanical response of ZrCu-based bulk metallic glasses. Int J Mech Sci 2021;211:106770. https://doi.org/10.1016/j.ijmecsci.2021.106770.
[22] Zhao Y, Lu J, Zhang Y, Wu F, Huo D. Development of an analytical model based on Mohr–Coulomb criterion for cutting of metallic glasses. Int J Mech Sci 2016;106:168–75. https://doi.org/10.1016/j.ijmecsci.2015.12.016.
[23] Şopu D, et al. Structure-property relationships in nanoporous metallic glasses. Acta Mater 2016;106:199–207. https://doi.org/10.1016/j.actamat.2015.12.026.
[24] Yu J, et al. Nanoporous metals by dealloying multicomponent metallic glasses. Chem Mater 2008;20:4548–50. https://doi.org/10.1021/cm8009644.
[25] Inoue A, Wada T, Louzguine-Luzgin DV. Improved mechanical properties of bulk glassy alloys containing spherical pores. Mater Sci Eng A 2007;471:144–50. https://doi.org/10.1016/j.msea.2006.10.172.
[26] Wada T, Inoue A, Greer AL. Enhancement of room-temperature plasticity in a bulk metallic glass by finely dispersed porosity. Appl Phys Lett 2005;86:251907. https://doi.org/10.1063/1.1953884.
[27] Zhao P, Li J, Wang Y. Heterogeneously randomized STZ model of metallic glasses: softening and extreme value statistics during deformation. Int J Plast 2013;40:1–22. https://doi.org/10.1016/j.ijplas.2012.06.007.

[28] Luo Y, Yang G, Shao Y, Yao K. The effect of void defects on the shear band nucleation of metallic glasses. Intermetallics 2018;94:114–8. https://doi.org/10.1016/j.intermet.2017.12.026.

[29] Ritter Y, Şopu D, Gleiter H, Albe K. Structure, stability and mechanical properties of internal interfaces in Cu64Zr36 nanoglasses studied by MD simulations. Acta Mater 2011;59:6588–93. https://doi.org/10.1016/j.actamat.2011.07.013.

[30] Adibi S, Branicio P, Zhang YW, Joshi S. Composition and grain size effects on the structural and mechanical properties of CuZr nanoglasses. J Appl Phys 2014;116: 043522. https://doi.org/10.1063/1.4891450.].

[31] Wang C, et al. Tuning the Curie temperature of Fe90Sc10 nanoglasses by varying the volume fraction and the composition of the interfaces. Scr Mater 2019;159: 109–12. https://doi.org/10.1016/j.scriptamat.2018.09.025.

[32] Ma E, Zhu T. Towards strength–ductility synergy through the design of heterogeneous nanostructures in metals. Mater Today 2017;20:323–31. https://doi.org/10.1016/j.mattod.2017.02.003.

[33] Yuan S, Branicio PS. Tuning the mechanical properties of nanoglass-metallic glass composites with brick and mortar designs. Scr Mater 2021;194:113639. https://doi.org/10.1016/j.scriptamat.2020.113639.

[34] Song J, Zhu W, Wei X. Correlations between the hierarchical spatial heterogeneity and the mechanical properties of metallic glasses. Int J Mech Sci 2021;204:106570. https://doi.org/10.1016/j.ijmecsci.2021.106570.

[35] Khmich A, Hassani A, Sbiaai K, Hasnaoui A. Tuning of mechanical properties of Tantalum-based metallic glasses. Int J Mech Sci 2021;204:106546. https://doi.org/10.1016/j.ijmecsci.2021.106546.

[36] Sha ZD, et al. Strong and superplastic nanoglass. Nanoscale 2015;7:17404–9. https://doi.org/10.1039/c5nr04740d.

[37] Albe K, Ritter Y, Şopu D. Enhancing the plasticity of metallic glasses: shear band formation, nanocomposites and nanoglasses investigated by molecular dynamics simulations. Mech Mater 2013;67:94–103. https://doi.org/10.1016/j.mechmat.2013.06.004.

[38] Peng CX, et al. Deformation behavior of designed dual-phase CuZr metallic glasses. Mater Des 2019;168:107662. https://doi.org/10.1016/j.matdes.2019.107662.

[39] Cheng Z, Zhou H, Lu Q, Gao H, Lu L. Extra strengthening and work hardening in gradient nanotwinned metals. Science 2018;362:eaau1925. https://doi.org/10.1126/science.aau1925.

[40] Wang Y, Li M, Xu J. Free volume gradient effect on mechanical properties of metallic glasses. Scr Mater 2017;130:12–6. https://doi.org/10.1016/j.scriptamat.2016.11.003.

[41] Yuan S, Branicio PS. Gradient microstructure induced shear band constraint, delocalization, and delayed failure in CuZr nanoglasses. Int J Plast 2020;134: 102845. https://doi.org/10.1016/j.ijplas.2020.102845.

[42] Zhao L, et al. Simultaneous improvement of plasticity and strength of metallic glasses by tailoring residual stress: Role of stress gradient on shear banding. Mater Des 2021;197:109246. https://doi.org/10.1016/j.matdes.2020.109246.

[43] Hammond KD. Parallel point defect identification in molecular dynamics simulations without post-processing: a compute and dump style for LAMMPS. Comput Phys Commun 2020;247:106862. https://doi.org/10.1016/j.cpc.2019.106862.

[44] Mendelev MI, Sun Y, Zhang F, Wang CZ, Ho KM. Development of a semi-empirical potential suitable for molecular dynamics simulation of vitrification in Cu-Zr alloys. J Chem Phys 2019;151:214502. https://doi.org/10.1063/1.5131500.

[45] Cheng YQ, Cao AJ, Sheng HW, Ma E. Local order influences initiation of plastic flow in metallic glass: effects of alloy composition and sample cooling history. Acta Mater 2008;56:5263–75. https://doi.org/10.1016/j.actamat.2008.07.011.

[46] Lee M, Lee CM, Lee KR, Ma E, Lee JC. Networked interpenetrating connections of icosahedra: Effects on shear transformations in metallic glass. Acta Mater 2011;59: 159–70. https://doi.org/10.1016/j.actamat.2010.09.020.

[47] Feng S, et al. Atomic structure of shear bands in Cu64Zr36 metallic glasses studied by molecular dynamics simulations. Acta Mater 2015;95:236–43. https://doi.org/10.1016/j.actamat.2015.05.047.

[48] Mauro N, et al. Short- and medium-range order in Zr80Pt20 liquids. Phys Rev B 2011;83:1841091–8. https://doi.org/10.1103/PhysRevB.83.184109.

[49] Guan Y, Song W, Wang Y, Liu S, Yu Y. Dynamic responses in shocked Cu-Zr nanoglasses with gradient microstructure. Int J Plast 2022;149:103154. https://doi.org/10.1016/j.ijplas.2021.103154.

[50] Guan YL, Dai LS, Shao JL, Song WD. Molecular dynamics study on the nanovoid collapse and local deformation in shocked Cu50Zr50 metallic glasses. J NonCryst Solids 2021;559:120703. https://doi.org/10.1016/j.jnoncrysol.2021.120703.

[51] Hu YC, Li FX, Li MZ, Bai HY, Wang WH. Five-fold symmetry as indicator of dynamic arrest in metallic glass-forming liquids. Nat Commun 2015;6:8310. https://doi.org/10.1038/ncomms9310.

[52] Wang PF, et al. Atomic structure evolution of (CuZr)100-xAgx glass under compression deformation. J Alloy Compd 2019;777:44–51. https://doi.org/10.1016/j.jallcom.2018.08.213.

[53] Pan S, et al. Bond-breaking analyses on the characteristics of flow defects in metallic glasses under plastic deformation. J Alloy Compd 2019;799:450–61. https://doi.org/10.1016/j.jallcom.2019.05.195.

[54] Shimizu F, Ogata S, Li J. Theory of shear banding in metallic glasses and molecular dynamics calculations. Mater Trans 2007;48:2923–7. https://doi.org/10.2320/matertrans.MJ200769.

[55] Spaepen F. A microscopic mechanism for steady state inhomogeneous flow in metallic glasses. Acta Metall 1977;25:407–15. https://doi.org/10.1016/0001-6160(77)90232-2.

[56] Turnbull D, Cohen M. Free-volume model of the amorphous phase: glass transition. J Chem Phys 1961;34:120–5. https://doi.org/10.1063/1.1731549.

[57] Yang L, et al. Atomic-scale mechanisms of the glass-forming ability in metallic glasses. Phys Rev Lett 2012;109:105502. https://doi.org/10.1103/PhysRevLett.109.105502.

[58] Gao Y. An implicit finite element method for simulating inhomogeneous deformation and shear bands of amorphous alloys based on the free-volume model. Model Simul Mater Sci Eng 2006;14:1329–45. https://doi.org/10.1088/0965-0393/14/8/001.

[59] Haruyama O, Inoue A. Free volume kinetics during sub-Tg structural relaxation of a bulk Pd40Ni40P20 metallic glass. Appl Phys Lett 2006;88. https://doi.org/10.1063/1.2189833.

[60] Huang R, Suo Z, Prevost J, Nix WD. Inhomogeneous deformation in metallic glasses. J Mech Phys Solids 2002;50:1011–27. https://doi.org/10.1016/S0022-5096(01)00115-6.

[61] Şopu D, Stukowski A, Stoica M, Scudino S. Atomic-level processes of shear band nucleation in metallic glasses. Phys Rev Lett 2017;119. https://doi.org/10.1103/PhysRevLett.119.195503.

[62] Şopu D, Scudino S, Bian XL, Gammer C, Eckert J. Atomic-scale origin of shear band multiplication in heterogeneous metallic glasses. Scr Mater 2020;178:57–61. https://doi.org/10.1016/j.scriptamat.2019.11.006.

[63] Tang Y, et al. Extra plasticity governed by shear band deflection in gradient metallic glasses. Nat Commun 2022;13:2120. https://doi.org/10.1038/s41467-022-29821-4.

[64] Kim HK, Lee M, Lee KR, Lee JC. How can a minor element added to a binary amorphous alloy simultaneously improve the plasticity and glass-forming ability? Acta Mater 2013;61:6597–608. https://doi.org/10.1016/j.actamat.2013.07.044.

[65] Klement W, Willens RH, Duwez POL. Non-crystalline structure in solidified gold–silicon alloys. Nature 1960;187:869–70. https://doi.org/10.1038/187869b0.

[66] Jing Q, Liu RP, Shao GJ, Wang WK. Preparation and super-plastic deformation of the Zr-based bulk metallic glass. Mater Sci Eng: A 2003;359:402–4. https://doi.org/10.1016/S0921-5093(03)00370-8.

[67] Ma J, et al. Fast surface dynamics enabled cold joining of metallic glasses. Sci Adv 2019;5:eaax7256. https://doi.org/10.1126/sciadv.aax7256.

[68] Li X, et al. Ultrasonic plasticity of metallic glass near room temperature. Appl Mater Today 2020;21:100866. https://doi.org/10.1016/j.apmt.2020.100866.

[69] Yang F, Wang C, Bai H, Wang W, Liu Y. Periodic island-layer-island growth during deposition of ultrastable metallic glasses. Commun Mater 2021;2:75. https://doi.org/10.1038/s43246-021-00180-9.

[70] Zhang C, Ouyang D, Pauly S, Liu L. 3D printing of bulk metallic glasses. Mater Sci Eng R Rep 2021;145:100625. https://doi.org/10.1016/j.mser.2021.100625.

[71] Guan S, et al. Additively manufactured CrMnFeCoNi/AlCoCrFeNiTi0.5 laminated high-entropy alloy with enhanced strength-plasticity synergy. Scr Mater 2020;183: 133–8. https://doi.org/10.1016/j.scriptamat.2020.03.032.